Characterizing hydrogen-fuelled pulsating combustion on thermodynamic properties of a combustor

Zhao, Dan; Guan, Yiheng; Reinecke, Arne

2019

Zhao, D., Guan, Y., & Reinecke, A. (2019). Characterizing hydrogen-fuelled pulsating combustion on thermodynamic properties of a combustor. Commuications Physics, 2(1), 44-. doi:10.1038/s42005-019-0142-8

https://hdl.handle.net/10356/141840

https://doi.org/10.1038/s42005-019-0142-8

COMMUNICATIONS PHYSICS

ARTICLE

https://doi.org/10.1038/s42005-019-0142-8 OPEN

Characterizing hydrogen-fuelled pulsating combustion on thermodynamic properties of a combustor

Dan Zhao [1], Yiheng Guan[2] & Arne Reinecke[3]

Unlike hydrocarbon fuel, hydrogen is 'green' and attracting more and more attentions in energy and propulsion sectors due to the zero emission of CO and CO_2. By applying numerical simulations, we explore the physics of how a hydrogen-burnt flame can sustain pulsating combustion and its impact on the thermodynamic properties of a standing-wave combustor. We also explain how implementing a heat exchanger can mitigate such pulsating combustion. The dynamic interactions of the unsteady flow-flame-acoustics-heater are examined by varying the mass flow rate $\dot{m}_{H2}$ and the heating bands' surface temperature T_H. The frequency and amplitude of the pulsating combustion are shown to depend strongly on $\dot{m}_{H2}$. In addition, varying T_H is shown to lead to not only the molar fraction of the combustion species being changed but also the flame-sustained pulsating oscillations being mitigated somehow. Finally, nonlinearity is observed and identified in the unsteady flow velocity and the two heat sources.

[1] Department of Mechanical Engineering, College of Engineering, University of Canterbury, Private Bag 4800, Christchurch 8140, New Zealand. [2] School of Energy and Power Engineering, Jiangsu University of Science and Technology, Mengxi Rd 2, 212003 Zhenjiang City, Jiangsu Province, China. [3] College of Engineering, Nanyang Technological University, 50 Nanyang Avenue, Singapore 639798, Singapore. Correspondence and requests for materials should be addressed to D.Z. (email: dan.zhao@canterbury.ac.nz)

Combustion instability is an undesirable phenomenon that occurs frequently in lean premixed combustion systems for power generation or propulsion[1–3]. Typically, it results from dynamic interactions between acoustics and premixed turbulent[4] and laminar flames[5]. Combustion instability could be characterized by a loudly 'singing' and violently 'dancing' flame in longitudinal or azimuthal direction (mode). Longitudinal-type instability has been intensively studied[6]. The dominant thermoacoustic instability is experimentally shown to switch by observing a shift from a low- to a high-frequency 'tone'. When combustion instability occurs[7,8], it can cause severe vibration, overheating, flame flashback, and decreased performance[9]. In severe cases, the engines, propellant systems and structures could be damaged.

Intensive research has been conducted on hydrogen-involved combustion instability. Matsuyama et al.[10] conducted LES (large eddy simulations) on a single-element atmospheric combustor. It is found that the primary driving mechanism of 1k Hz combustion instability is the acoustically coupled pulsating motion of the inner H_2/O_2 flame or periodic ignition of H_2/O_2 mixture. Recently, Hemchandra et al.[11] discovered that there are two different mechanisms driving combustion instability. One is a strong coupling between acoustics and hydrodynamic modes. The other one is a weak coupling resulting in semi-open-loop forcing of the flame by a self-sustained hydrodynamic mode. Urbano and Selle[12] analyzed transverse combustion instabilities in a reduced-scale rocket motor. The interaction between acoustics and vorticity is found to be the main damping mechanism for coaxial H_2/O_2 flame-sustained instability. Injector-driven combustion instabilities are experimentally observed in a hydrogen/oxygen rocket motor[13]. The observed instabilities are a result of the interaction between the injector resonant frequencies and the combustion chamber resonant frequencies.

Combustion instability may be mitigated by applying two classical means. One is passive control. Kim et al.[14] experimentally evaluated the attenuation effect of sponge-like porous medium on combustion instability in a lab-scale swirl combustor. It is found that up to 40% of pressure attenuation is achievable. A perforated plate/liner[15] is analytically studied on damping combustion instability in an annular combustor[16]. Tao et al.[16] show that a cooling/bias flow can enhance the acoustic damping effect of such perforated plates/liners. The damping performance is found to be optimized at Strouhal number near 0.3. Similar stabilization effects are observed on perforated slits on a modelled combustor[17]. Wu et al.[18] actively tuned the acoustic damping of a Helmholtz resonator to mitigate combustion instability in a Y-shaped Rijke tube. Approximately 60 dB sound pressure level (SPL) reduction is achieved by actively tuning the resonator's back-wall. Similar implementation of a Helmholtz resonator[19] is conducted on a Rijke tube[20].

The other approach is active control using a developed controller. Phase-shift or PI (proportional-integral) controller is the typical one that is applied to suppress combustion instabilities by using loudspeakers[21,22]. An excellent review on active control of combustion instability can be found in refs. [23,24]. In addition to the classical active and passive control approaches, alternative means have been proposed and tested. For example, Jocher et al.[25] experimentally confirm that combustion instability could be controlled in open-loop configuration by applying a magnetic field via reducing the growth rate of flame perturbations. Henderson and Xu[26] experimentally study the effect of applying direct-current electric field on damping thermoacoustic instability in a horizontal Rijke tube. Approximately 20 dB SPL reduction is achieved. Combustion instability is mitigated by actuating a swirler in a premixed methane-fuelled combustor[27]. It is found that creating a higher-intensity turbulence and a swirl flow can alter the flame position and structure, and so the combustor stability behaviours.

Fuel composition is found to play an important role in generating and suppressing combustion instability. Diao et al.[28] experimentally study the flame–acoustics interaction in a rectangular H_2/O_2 shear-coflow combustor with CH_4 actively blended. It is found that heat release oscillations are significantly dampened, when gaseous methane is blended with gaseous hydrogen. The effect of blending methane with hydrogen on combustion instability is experimentally studied[29] on a swirl combustor. It is found that increasing hydrogen concentration (up to 30% in volume) in the fuel leads to enhanced responses of the flame at non-resonant frequencies. Choi and Lee[30] found that when hydrogen is added into syngas both acoustic pressure, unsteady heat release respond sensitively and nonlinearly. Similar combustion instability studies of $H_2/CO/CH_4$ syngases were conducted on a partially premixed gas turbine combustor[31]. H_2 contents are identified to play an important role in producing higher-order (higher frequency) instability mode and mode-shifting. Acoustic measurements of a lean premixed combustor with hydrogen and methane or propane fuelled confirm the key role of hydrogen in producing higher sound -pressure-level instability[32]. The effects of fuel composition on a premixed gas turbine combustion are well reviewed in ref. [33], with emphasis being placed on combustion system stability[34,35] and emissions.

To the best knowledge of the authors, there are few reports in the literature discussing the physics and mechanisms underlying hydrogen-fuelled pulsating combustion, and its impact on the thermodynamic properties of a standing-wave combustor. In addition, there is a lack of alternate but effective means for preventing or mitigating combustion instability. In this work, an acoustically open−open premixed combustor fuelled with hydrogen–air mixture and a constant-temperature heat exchanger is numerically studied to shed light on the dynamic flame−acoustics−heater interaction. The hydrogen mass flow rate $\dot{m}_{H_2}$ and the surface temperature T_H of the heating bands are evaluated. It is found that varying T_H can lead to partial or complete change in the molar fraction of the combustion species and the mitigation in the flame-sustained pulsating oscillations. Finally, nonlinearity is identified and observed on these heat sources.

Results

Effect of mass flow rate $\dot{m}_{H_2}$. As the mixture of the hydrogen and air is burned, a conical shaped flame is confined in the combustor. Figure 1 shows the turbulent reaction rate as the hydrogen mass flow rate $\dot{m}_{H_2}$ is set to three different values. It can be seen that the flame length and the surface area are dramatically increased, and so is the heat release. As it is well known that unsteady heat release is an energy-efficient monopole-like sound source, acoustic pressure disturbances are generated with a small amplitude initially. However, whether the acoustic disturbances will grow into limit cycle pulsating combustion oscillations needs to be examined.

The effect of the flame on producing pulsating pressure oscillations is shown in Fig. 2. Figure 2a shows the time evolution of the acoustic pressure fluctuations at the midpoint of the combustor in the axial direction, as the hydrogen mass flow rate $\dot{m}_{H_2}$ is set to 1.0×10^{-5} kg s^{-1}. It can be seen that there are small-amplitude pressure disturbances initially. However, such distances grow quickly into a limit cycle. Figure 2b shows the corresponding phase diagram of the pressure fluctuations. The circle shape characterizes the limit cycle oscillations in phase plot. Figure 2c illustrates the phase diagram of the acoustic pressure, as the mass

flow rate $\dot{m}_{H_2}$ of the hydrogen is set to $5.0 \times 10^{-6}\,\mathrm{kg\,s^{-1}}$. It can be seen that a limit cycle is also produced. However, the amplitude is approximately 50% of that at $\dot{m}_{H_2} = 1.0 \times 10^{-5}\,\mathrm{kg\,s^{-1}}$. Further decreasing $\dot{m}_{H_2}$ leads to a reduction in the amplitude of the pulsating oscillation, as shown in Fig. 2d.

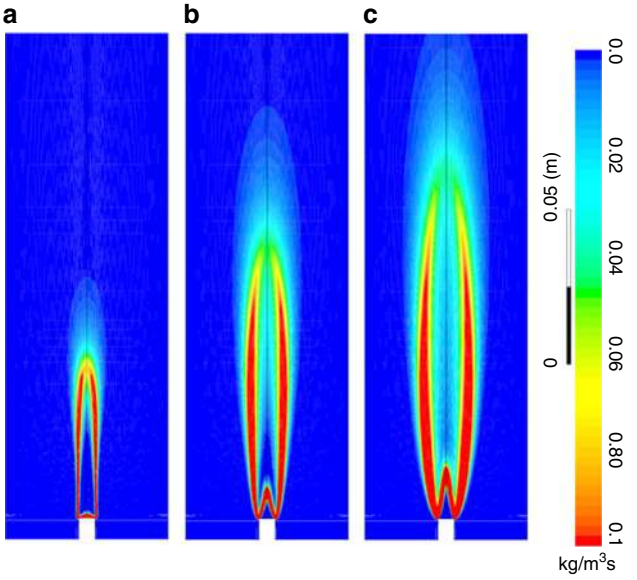

Fig. 1 Calculated turbulent reaction rate of the hydrogen-fuelled flame, as the hydrogen mass flow rate $\dot{m}_{H_2}$ is set to **a** $\dot{m}_{H_2} = 1.0 \times 10^{-6}\,\mathrm{kg\,s^{-1}}$, **b** $\dot{m}_{H_2} = 5.0 \times 10^{-6}\,\mathrm{kg\,s^{-1}}$ and **c** $\dot{m}_{H_2} = 1.0 \times 10^{-5}\,\mathrm{kg\,s^{-1}}$

Unlike hydrocarbon fuels, hydrogen is a nonhydrocarbon that exhibits the largest mass diffusivity features. Figure 3 compares the profiles of the reactants and combustion product species in both axial and radial directions, as the hydrogen mass flow rate $\dot{m}_{H_2}$ is set to three different values. The red colour curves show the major hydrogen distribution. Along the axial direction (see Fig. 3a–c) the mole fraction begins to decay sharply; complete depletion of the hydrogen is achieved after the reaction zone. In the radial direction, this finding is consistent with the variation of $\dot{m}_{H_2}$. The mole fraction profile of H_2O is observed to vary dramatically in the axial direction, as the hydrogen mass flow rate is changed (see the blue colour curves in Fig. 3a–c). As $\dot{m}_{H_2}$ is decreased from 1.0×10^{-5} to $1.0 \times 10^{-6}\,\mathrm{kg\,s^{-1}}$, the separation between the preheat and reaction zones becomes more sharp. In other words, the wave/peak thickness, i.e. the maximum molar fraction region, is reduced. At $t = 2.0$ s, large-amplitude pulsating oscillations are produced by burning the mixture of H_2 and O_2 in the open−open tube. Such pulsating fluctuations propagate along the combustor and the fuel tube. They in turn affect the local molar fractions of the species such as H_2 and H_2O.

The profile of O_2 is almost the same in the axial direction, as $\dot{m}_{H_2}$ is varied. It is injected from the Bunsen burner, and so its mole fraction is increased gradually from the pre-reacting zone to the reacting zone and the after-reaction zone, and is finally 'saturated'. As far as the radial profiles (see Fig. 3d–f) are concerned, they are similar in shape for Fig. 3d, f, and in the growth rate for Fig. 3e. The shape profiles are similar especially near the inner surface of the tube. The maximum mole fraction of H_2 is reduced, and so is the thickness of the wave/peak of the water (H_2O) profile. The hydrogen mole fraction begins

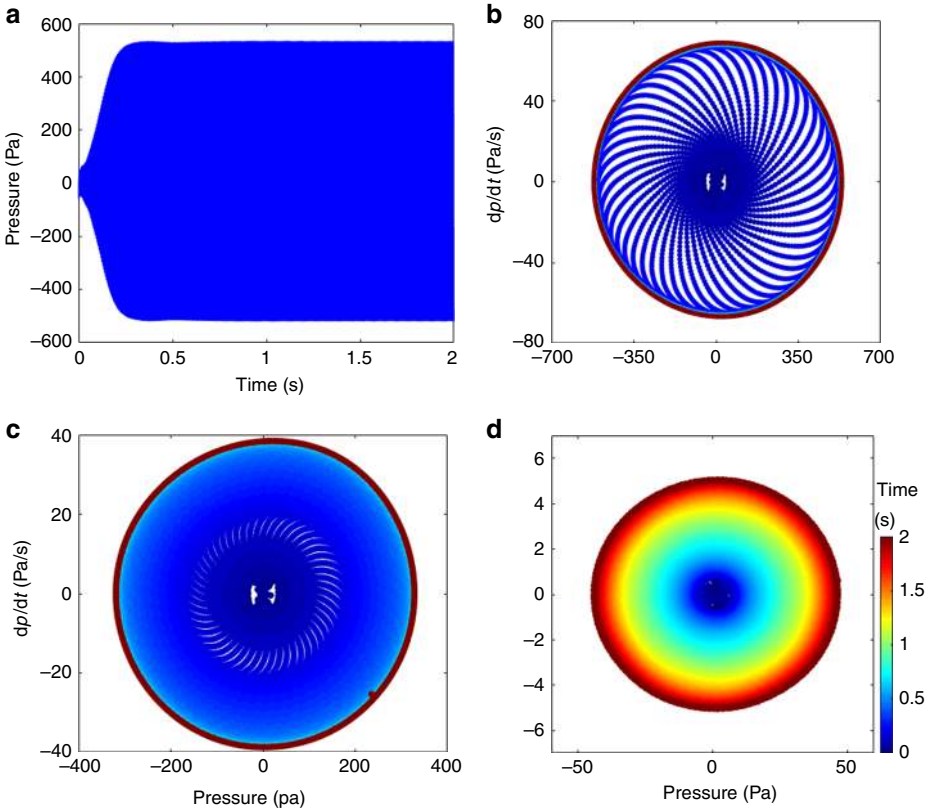

Fig. 2 Acoustic pressure fluctuations. **a** time evolution of the acoustic pressure at $\dot{m}_{H_2} = 1.0 \times 10^{-5}\,\mathrm{kg\,s^{-1}}$, **b** phase diagram of the pressure fluctuations at $\dot{m}_{H_2} = 1.0 \times 10^{-5}\,\mathrm{kg\,s^{-1}}$, **c** phase diagram of the pressure fluctuations at $\dot{m}_{H_2} = 5.0 \times 10^{-6}\,\mathrm{kg\,s^{-1}}$, **d** phase diagram of the pressure fluctuation, at $\dot{m}_{H_2} = 1.0 \times 10^{-6}\,\mathrm{kg\,s^{-1}}$

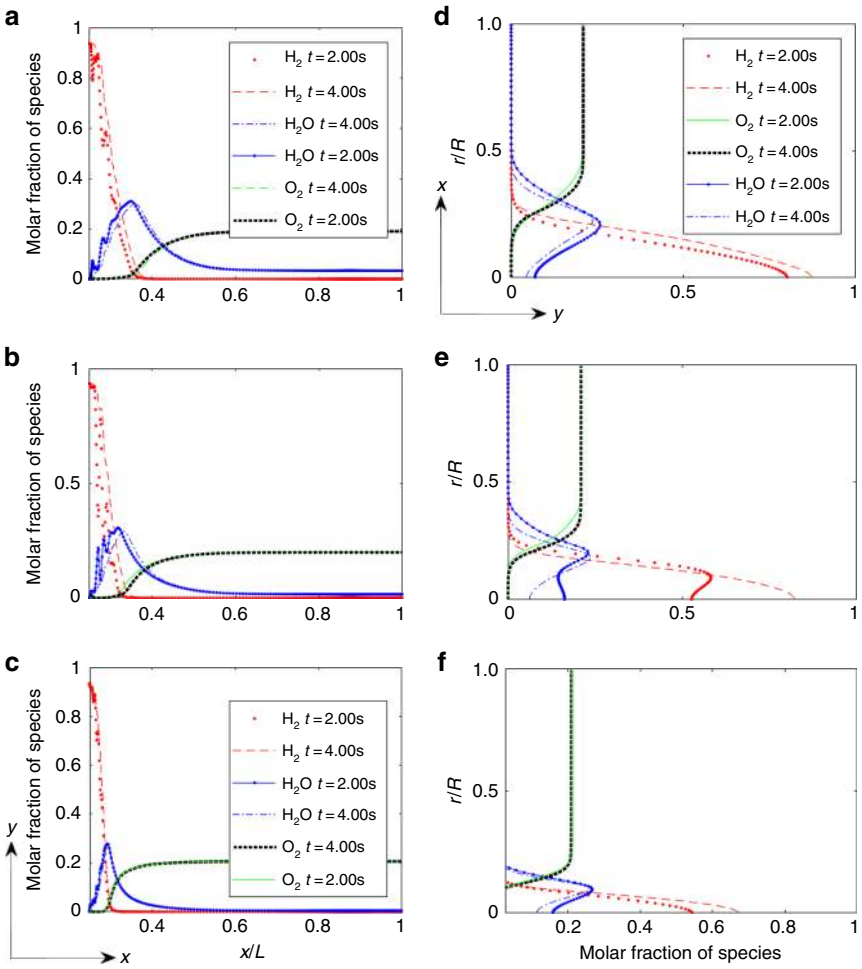

Fig. 3 Variation of the molar fraction of combustion species in the axial and radial directions. **a** $\dot{m}_{H_2} = 1.0\times10^{-5}\,\mathrm{kg\,s^{-1}}$, **b** $\dot{m}_{H_2} = 5.0\times10^{-6}\,\mathrm{kg\,s^{-1}}$, **c** $\dot{m}_{H_2} = 1.0\times10^{-6}\,\mathrm{kg\,s^{-1}}$, **d** $\dot{m}_{H_2} = 1.0\times10^{-5}\,\mathrm{kg\,s^{-1}}$, **e** $\dot{m}_{H_2} = 5.0\times10^{-6}\,\mathrm{kg\,s^{-1}}$, and **f** $\dot{m}_{H_2} = 1.0\times10^{-6}\,\mathrm{kg\,s^{-1}}$

to decrease from the point $r/R = 0$ and it becomes much sharper, as $\dot{m}_{H_2}$ is reduced to $\dot{m}_{H_2} = 1.0\times10^{-6}\,\mathrm{kg\,s^{-1}}$. In general, H_2, O_2 and H_2O are all a function of the spatial distance through the flame. Both water and hydrogen exist in the preheat zone. Note that more complicated 21-step chemical reactions are studied, as discussed in Supplementary Note 1. The new results with the 21 chemical reaction mechanisms/steps are provided in Supplementary Table 1. Comparison is made between the multiple-step and the much-simplified one-step reaction in terms of the temperature and velocity contours, and the combustion-driven pressure and the heat of reaction pulsating oscillations. Interested readers can find more details in Supplementary Figs. 1 and 2, and insightful discussion in Supplementary Note 1.

As the mixture of the hydrogen and air is burned, the instantaneous temperature at the midpoint of the combustor in the axial direction is monitored in real time. This is shown in Fig. 4 with $\dot{m}_{H_2}$ being set to three different values. It can be seen from Fig. 4a–c that the temperature is decreased dramatically, as $\dot{m}_{H_2}$ is decreased. The temperature fluctuates dramatically before the limit cycle oscillations are produced by the flame, i.e. $t \le 0.5$ s. However, with limit cycles being completely generated at $t \ge 1.0$ s, the temperature seems to be 'saturated'. To gain insight into the fluctuations of the temperature, a phase diagram of the instantaneous temperature $T(t)$ is plotted, as shown in Fig. 4d–f. It can be clearly seen that the gradient of the temperature, i.e. dT/dt, is non-zero. This means that the temperature is periodically oscillating around its mean value. Furthermore, the oscillation amplitude is dramatically reduced with a decrease in $\dot{m}_{H_2}$ (Fig. 4d–f). Finally, the fluctuating trend of the temperature reveals that the heat-to-acoustics energy conversion is nonirreversible.

The mode shapes of the acoustic pressure fluctuations are determined, and are discussed in Supplementary Note 2 (shown in Supplementary Fig. 3). Comparison is then made with the case of using CH_4 as the fuel. It is shown that the maximum pressure amplitude is observed near the mid-point of the combustor in the axial direction. A pressure node is expected at the combustor outlet, no matter whether CH_4 or H_2 is fuelled.

Effect of the heating bands. Heating bands with a constant surface temperature are implemented, aiming to dampen and/or prevent the onset of the flame-sustained pulsating oscillations. Time evolution of the pressure fluctuations as the temperature of the heating bands is increased from 300 to 1300 K at $t = 2.0$ s is shown in Fig. 5a, as $\dot{m}_{H_2}$ is set to three different values. It can be seen that as the hydrogen mass flow rate is greater than $\dot{m}_{H_2} = 5.0\times10^{-6}\,\mathrm{kg\,s^{-1}}$, increasing the temperature of the heating bands leads to a mitigation in the limit cycle oscillations. However, when the hydrogen mass flow rate is reduced to $\dot{m}_{H_2} = 1.0\times10^{-6}\,\mathrm{kg\,s^{-1}}$, actuating the heating bands is found to successfully prevent the onset of the limit cycle oscillations, as

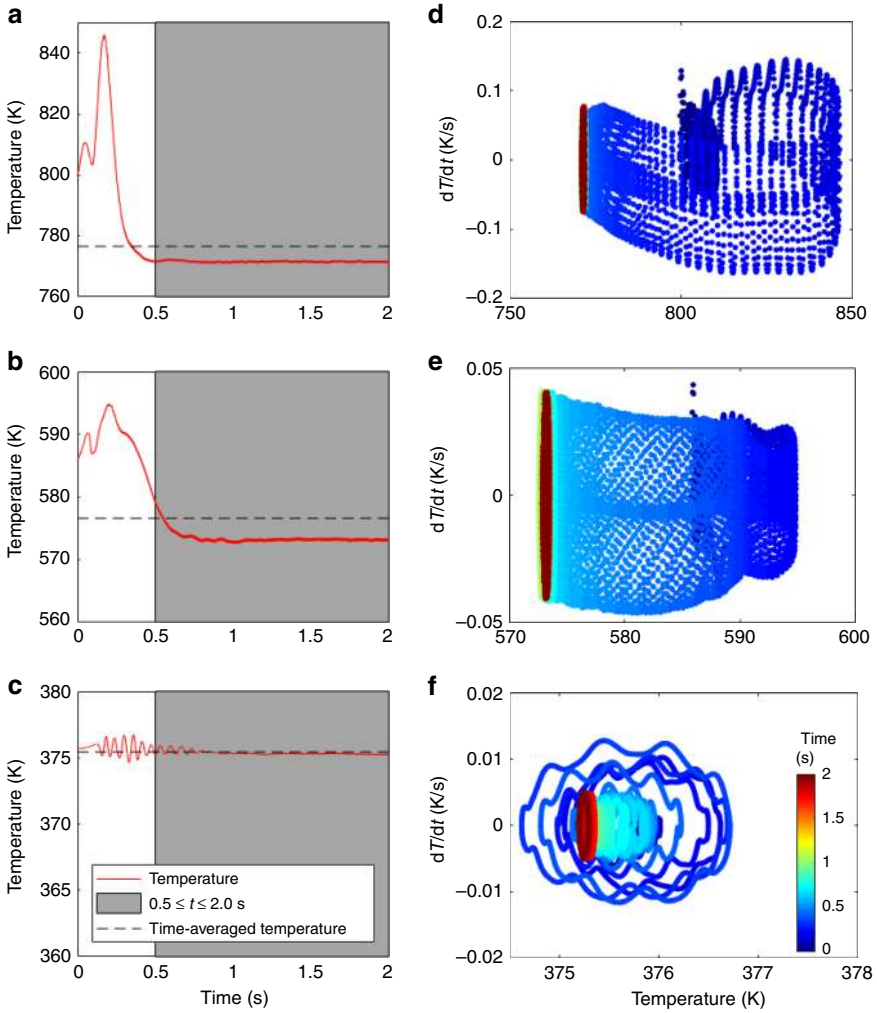

Fig. 4 Temperature fluctuation with time and its corresponding phase diagram. **a**–**c** Time evolution of the instantaneous temperature at the midpoint of the combustor, **d**–**f** the corresponding phase diagram to illustrate the periodic fluctuating characteristics. **a**, **d** $\dot{m}_{H_2} = 1.0 \times 10^{-5}\,\mathrm{kg\,s^{-1}}$, **b**, **e** $\dot{m}_{H_2} = 5.0 \times 10^{-6}\,\mathrm{kg\,s^{-1}}$, **c**, **f** $\dot{m}_{H_2} = 1.0 \times 10^{-6}\,\mathrm{kg\,s^{-1}}$

denoted by the solid green colour cure in Fig. 5a. To quantify the damping effect of the heating bands, the instantaneous acoustical energy $E_a(t)$ per unit volume of the combustor is determined:

$$E_a(t) = \frac{\frac{\omega}{2\pi}\int_t^{t+2\pi/\omega}[p'(t)]^2 \mathrm{d}t}{2\gamma p_0}, \qquad (1)$$

where $p'(t)$ is the acoustic pressure fluctuation, ω is the oscillation frequency, $\gamma = 1.4$ is the specific heat ratio, and $p_0 = 1.01325 \times 10^5$ Pa is the mean pressure. Note that the total acoustical energy E_a^{tot} at a given time can be determined by integrating $E_a(t)$ over the entire combustor volume. If a 3D cylindrical coordinate is considered, then $E_a^{tot}(t) = \int_0^{2\pi} \mathrm{d}\vartheta \int_0^R r\mathrm{d}r \int_0^L E_a(t)\,\mathrm{d}x$. Since the combustor volume is specified with the constant cross-sectional area and the axial length L, E_a can be applied to characterize the intensity of combustion oscillations.

Time evolution of the acoustical energy E_a is shown in Fig. 5b as $\dot{m}_{H_2}$ is set to three different values. It can be seen that as $\dot{m}_{H_2} = 1.0 \times 10^{-5}\,\mathrm{kg\,s^{-1}}$, the acoustical energy E_a is reduced by 61.7% from $t = 2.0$ s to $t = 4.0$ s. Approximately 81% acoustical energy reduction is achieved at $\dot{m}_{H_2} = 5.0 \times 10^{-6}\,\mathrm{kg\,s^{-1}}$. At $\dot{m}_{H_2} = 1.0 \times 10^{-6}\,\mathrm{kg\,s^{-1}}$, the pressure fluctuations are successfully prevented from growing into limit cycles, as observed for $\dot{m}_{H_2} = 5.0 \times 10^{-6}\,\mathrm{kg\,s^{-1}}$ and $\dot{m}_{H_2} = 1.0 \times 10^{-5}\,\mathrm{kg\,s^{-1}}$. This confirms that the heating bands are applicable to dampen flame-sustained pulsating oscillations.

Time-frequency analysis is conducted to study the heat of reaction of the hydrogen-fuelled flame and the total heat fluxes of the heating bands before and after changing the temperature of the heating bands (Fig. 6). It can be seen that the nonlinearity is associated with the heat release rates of the flame and the heating bands, due to the comparable frequency peaks. Before the heating bands' temperature is changed, i.e. $t \le 2$ s, the heat release of the flame is associated with multiple modes at different frequencies. The dominant mode frequency is approximately 204 Hz (see Fig. 5a). However, the harmonic modes are excited as the heating bands' temperature is increased to 1300 K at $2.0 < t \le 4.0$ s.

Nonlinearity characteristics of the combustion system are further identified by conducting the frequency spectrum analysis of the flow velocity. This is shown in Fig. 7, as the hydrogen mass flow rate $\dot{m}_{H_2}$ is set to three different values. Figure 7a–c shows the time evolution of the instantaneous velocity. It can be seen that as $\dot{m}_{H_2}$ is decreased, with no change in the temperature of the heating bands ($t \le 2.0$ s), the mean velocity is reduced from 3.1 to 1.53 m s^{-1}. The amplitude of the velocity fluctuation is also decreased dramatically. Figure 7d–f illustrates the frequency

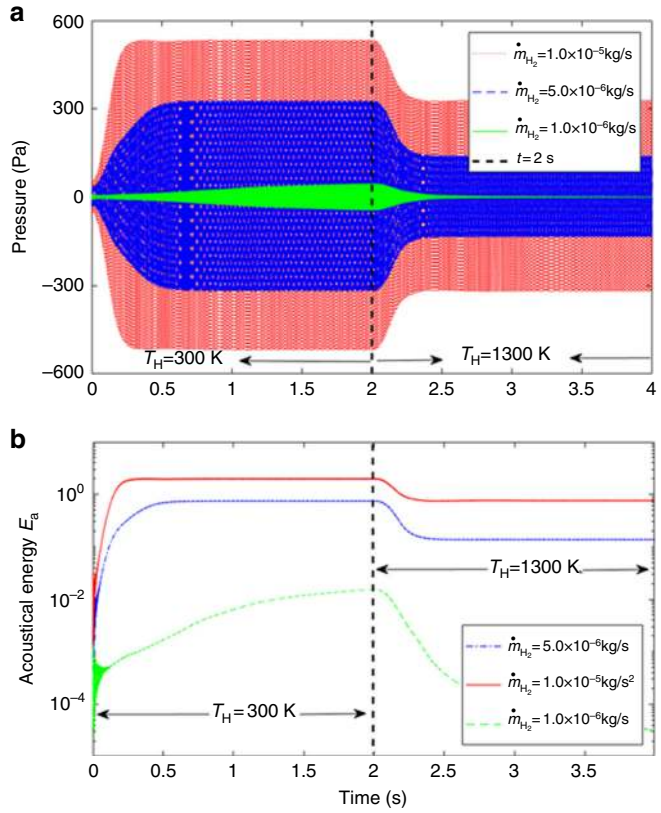

Fig. 5 Acoustic pressure and acoustical energy variation with time. **a** Time evolution of the pressure fluctuations, **b** time evolution of the acoustical energy, as the hydrogen mass flow rate $\dot{m}_{H_2}$ is set to three different values, and the surface temperature of the heating bands is suddenly increased from 300 to 1300 K at $t = 2.0$ s. Mathematically, $T_H = 300$ at $t \le 2.0$ and $T_H = 1300$ K at $2.0 < t \le 4.0$ s

spectrum of the velocity fluctuation, before and after the temperature of the heating bands is changed. It can be seen that ~4% of the dominant frequency shift occurs from $t \le 2.0$ to $t > 2.0$ s. A similar frequency shift is observed from 203.0 to 177.6 Hz, as the mass flow rate $\dot{m}_{H_2}$ is decreased from 1.0×10^{-5} to 1.0×10^{-6} kg s^{-1}. However, the dominant frequency shift is approximately 12.7%. This is most likely due to the fact that the H_2 mass flow rate and the total heat release are reduced. The mean temperature and the speed of sound in the combustor are also decreased. To maintain the standing-wave mode shape and to satisfy the inlet and outlet boundary conditions, the dominant frequency of the H_2-excited oscillations is thus decreased. In general, the flame-excited pulsating oscillation signature is found to depend strongly on the hydrogen mass flow rate.

The effect of the heating bands on combustion species is also examined, as shown in Fig. 3. Comparison is made before and after the surface temperature T_H of the heating bands is increased from 300 to 1300 K at $t = 2.0$ s. It can be seen from Fig. 3a–c that the mole fraction profiles of the reactants of H_2 and O_2, and the product H_2O at $T_H = 1300$ K are quite similar to those at $T_H = 300$ K in the axial direction. Furthermore, the thickness of 'the wave/peak' profile is also the same. This is most likely due to the negligible effect of the mean heat release of the heating bands on the hydrogen-fuelled flame, as they are placed far away downstream of the combustor. As shown in Fig. 3d–f, the radial profiles of the mole fraction of O_2 look quite similar, before and after T_H is changed. This is most likely due to the fact that the inner burner is associated with a mixture of hydrogen and air. In addition, there is a simultaneous flow of air injected from the bottom of the cylindrical tube (see Fig. 8). The mole fraction profiles of H_2 and H_2O, especially the maximum molar fraction of the species at $r/R = 0$, are however different. This may be due to the fact that the periodic combustion oscillations are dampened with the actuation of the heating bands, which affects the hydrogen and H_2O distribution along the radial direction. The oscillation intensity and frequency may contribute to the radial profiles variation of H_2 and H_2O.

As revealed by Rayleigh[1,2], limit cycle pulsating combustion occurs due to the unsteady heat release, and acoustic pressure fluctuations are in phase. In order to shed light on the dynamic flame−flow−heater interaction, Rayleigh index angle θ_{RI} is determined (Supplementary Note 3) to check whether the unsteady heat release from the flame Q'_f and the heating bands Q'_H are in or out of phase with the acoustic pressure fluctuations. θ_{RI} is defined as the phase difference between the heat release and the pressure fluctuation at the frequency ω at any instant. Supplementary Figures 4 and 5 show the time evolution of the phase difference between the acoustic disturbances and the unsteady heat release from the flame and the heater, respectively.

Discussion

We have numerically shown how hydrogen-fuelled flame can sustain self-excited pulsating oscillations, and its impact on the thermodynamic properties of a standing-wave combustor with heating bands confined. The physics behind the flame−acoustics −heater−flow interaction is numerically examined. It is found that the hydrogen mass flow rate $\dot{m}_{H_2}$ determines not only the pulsating combustion characteristics but also the molar fraction profiles of the combustion species. Approximately 13% of the dominant frequency shift is observed in the dominant mode. Furthermore, the combustor is found to be highly nonlinear in terms of the acoustic velocity and heat of reaction Q_f from the flame and the heat flux Q_H from the heating bands. Finally, varying the surface temperature T_H of the heating bands is shown to be able to successfully prevent the onset of limit cycle pulsating oscillations excited by the hydrogen-fuelled flame. By conducting further analyses on the mode shape and by determining the Rayleigh index angle it has been confirmed that, when limit cycle pulsating combustion occurs, the combustor is a standing-wave one. Rayleigh index angle reveals that the unsteady heat release constructively interacts with the acoustic disturbances in the flame, while destructive interactions are observed on the heating bands. This is consistent with the Rayleigh criterion and explains why the heating bands can be applied to dampen pulsating combustion oscillations. In addition, it is interesting to show that increasing the surface temperature of the heating bands leads to the combustion species profiles being varied. The present work sheds light on the fundamental physics and mechanism underlying hydrogen-fuelled combustion instability. It also opens up an alternative control means to dampen or to prevent the onset of the pulsating oscillations.

Methods

Model set-up. The geometry of the open−open standing-wave combustor is schematically shown in Fig. 8a. Hydrogen and air are injected into the combustor. The inner burner is associated with a mixture of the hydrogen and air. However, there is a simultaneous flow of air injected from the bottom of the cylindrical tube. Six heating bands (of length 30 mm) with the constant surface temperature are equally spaced in the radial direction. They are placed at a distance of L_h away from the top open end of the combustor. Note that these heating bands represent a classical heater consisting of distributed heating elements. We chose six heating bands here. Although the choice could have been three or four. A larger number of heating bands with a smaller surface area helps to keep the total heat release rate unchanged to achieve the effective control performance. Near the bottom open end

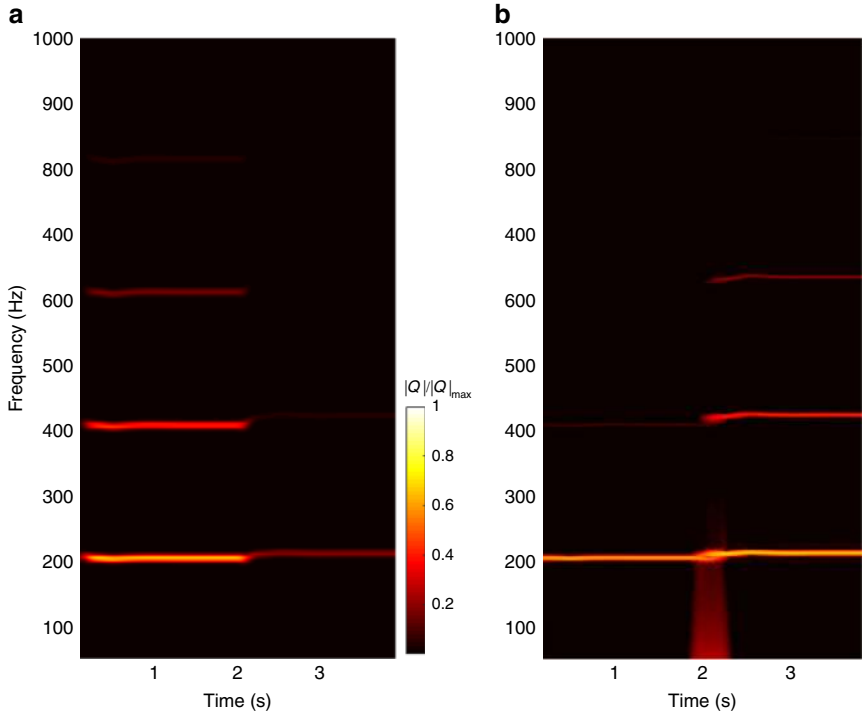

Fig. 6 Frequency spectrum of the heat of reaction of the hydrogen flame and the heat fluxes of the heating bands. **a** Time-frequency analysis of the heat of reaction of the flame and **b** the heat fluxes of the heating bands, as the hydrogen mass flow rate is set to $\dot{m}_{H_2} = 1.0 \times 10^{-5}\,\mathrm{kg\,s^{-1}}$, and the surface temperature of the heating bands is suddenly increased from 300 to 1300 K at $t = 2.0$. Mathematically, $T_H = 300$ at $t \le 2.0$ and $T_H = 1300$ K at $2 < t \le 4.0$ s

is a Bunsen burner with an inner diameter of 5.0 mm. The height of the Bunsen burner is L_b. The overall view of the 2D mesh generated by using Ansys ICEM CFD is shown in Fig. 8b. The mesh consists of 25,868 quadrilateral elements, 372 elements along the axis of the tube and 76 elements along the radius. Near the heating bands and the Bunsen burner, a finer grid is applied, as shown in Fig. 8b. The mesh is chosen on the basis of our mesh-independence study as discussed in Supplementary Note 4. The mesh-independence results are provided in Supplementary Figs. 6 and 7. Note that a 2D combustor is modelled for simplicity and for reducing the computational time and cost. However, a 3D modelled combustor is also investigated and compared with the 2D one for completeness, as discussed in Supplementary Note 5. This is shown in Supplementary Fig. 8. Approximately 16% difference is found between the pressure pulsation amplitudes predicted from the 2D and 3D combustors. However, the computational time is increased by 400%.

With the flame confined, there is an unsteady heat release and a mean flow results from the convection effect. In addition, unsteady heat release is an energy-efficient monopole-like acoustics source[36,37]. Acoustic distances are produced and propagated along the combustor. The interaction between the acoustic disturbances and the heating bands leads to further unsteady heat release. When the temperature of the mean flow is higher than the surface temperature of the heating bands, they absorb the heat released from the flame. Otherwise, heat is produced by the heating bands and transferred to the mean flow. The heat transfer process in our modelled combustor is unsteady. Thus, the current modelled combustor involves the dynamic interaction between the premixed flame, the unsteady flow, the acoustics and the heating bands.

Governing equations. The flame−acoustics−flow−heater interaction problem[38,39] is modelled by solving certain equations governing fluid dynamics and the chemical combustion reaction. All these equations need to be solved simultaneously and some of them are coupled, e.g. the fluid velocity will determine how the combustion species[40] will spread through the computational domain and at which particular locations in the numerical domain there might be more or less chemical reaction taking place.

The governing equations of mass, momentum, species fraction, energy conservations in the combustor are given as

$$\frac{\partial \rho}{\partial t} + \frac{\partial (\rho \mathbf{u}_i)}{\partial x_i} = 0, \tag{2}$$

$$\frac{\partial (\rho \mathbf{u}_i)}{\partial t} + \frac{\partial (\rho \mathbf{u}_i \mathbf{u}_j)}{\partial x_i} = -\frac{\partial p}{\partial t} + \frac{\partial}{\partial x_i}\left[\mu_t\left(\frac{\partial \mathbf{u}_i}{\partial x_j} + \frac{\partial \mathbf{u}_j}{\partial x_i}\right) - \frac{2}{3}\mu_t \frac{\partial \mathbf{u}_k}{\partial x_k}\right]\delta_{ij} + \rho g \delta_{i3}, \tag{3}$$

$$\frac{\partial (\rho \chi_k)}{\partial t} + \frac{\partial (\rho u_i \chi_k)}{\partial x_i} = \frac{\partial J_k}{\partial t} + R_k, \tag{4}$$

$$\frac{\partial (\rho E)}{\partial t} + \frac{\partial [u_i(\rho E + p)]}{\partial x_i} = \frac{\partial}{\partial x_j}\left(k_{\mathrm{eff}}\frac{\partial \mathrm{T}}{\partial x_j} - \sum_j h_j J_j + \mathbf{u}_i\left[\mu_{\mathrm{eff}}\left(\frac{\partial \mathbf{u}_j}{\partial x_i} + \frac{\partial \mathbf{u}_i}{\partial x_j}\right) - \frac{2}{3}\mu_{\mathrm{eff}}\frac{\partial \mathbf{u}_k}{\partial x_k}\delta_{ij}\right]\right), \tag{5}$$

where χ_k is the local mass fraction of the kth species, J_k is the diffusion flux of the kth species, R_k is the net rate of the kth species by chemical reaction, δ_{ij} denotes the Kronecker delta function and $\delta_{ij} = 1$ when $i = j$; otherwise $\delta_{ij} = 0$. The turbulent viscosity μ_t is introduced to model the effect of turbulence on the flow according to the Boussinesq hypothesis. This unknown needs to be determined via an additional modelling, for which the RNG $k-\varepsilon$ model in ANSYS Fluent is employed. The turbulent viscosity is computed from k, the turbulent kinetic energy, and ε, the turbulent dissipation, as given in the following expression:

$$\mu_t = 0.0845\rho\frac{k^2}{\varepsilon}. \tag{6}$$

The turbulent kinetic energy k and the dissipation rate ε are determined from the transport equations of similar structures to the governing equations for the fluid flow. They are given as

$$\frac{\partial (\rho k)}{\partial t} + \frac{\partial (\rho k \mathbf{u}_i)}{\partial x_i} = \frac{\partial}{\partial x_j}\left(\alpha_k \mu_{\mathrm{eff}}\frac{\partial k}{\partial x_j}\right) + G_k + G_b - \rho\varepsilon - Y_M \tag{7}$$

and

$$\frac{\partial (\rho \varepsilon)}{\partial t} + \frac{\partial (\rho \varepsilon \mathbf{u}_i)}{\partial x_i} = \frac{\partial}{\partial x_j}\left(\alpha_\varepsilon \mu_{\mathrm{eff}}\frac{\partial \varepsilon}{\partial x_j}\right) + C_{1\varepsilon}\frac{\varepsilon}{k}(G_k + C_{3\varepsilon}G_b) - C_{2\varepsilon}\rho\frac{\varepsilon^2}{k} - R_\varepsilon, \tag{8}$$

where G_k and G_b denote the production of turbulence kinetic energy resulting from the mean velocity gradient and buoyancy effects, respectively. Y_M describes part of the overall dissipation rate due to the fluctuation dilatation in compressible turbulence. The eddy-dissipation k–ε model is used to determine the production term R_k in Eq. (4). This production term is computed with the following expression:

$$R_k = \min\left(4.0\nu'_k \mathrm{MW}_k \rho\frac{\varepsilon}{k}\min_i\left(\frac{\chi_i}{\nu'_i M_i}\right), 2.0\nu'_k \mathrm{MW}_k \rho\frac{\varepsilon}{k}\frac{\sum_i \chi_i}{\sum_j^N \nu''_j \mathrm{MW}_j}\right), \tag{9}$$

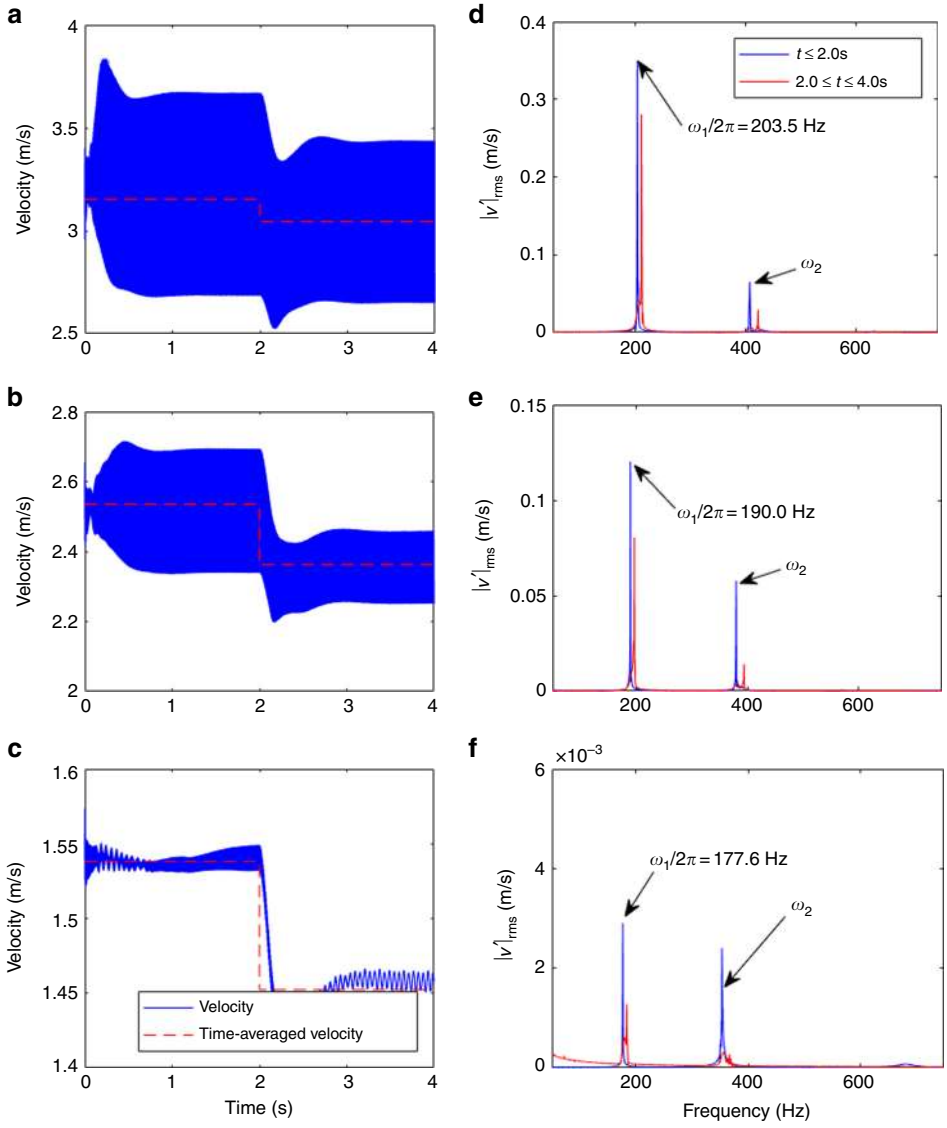

Fig. 7 Acoustic velocity variation with time and its corresponding frequency spectrum. **a**–**c** Time evolution of the instantaneous velocity fluctuations at the midpoint of the combustor and **d**–**f** the corresponding frequency spectrum. **a**, **d** $\dot{m}_{H_2} = 1.0 \times 10^{-5}\,\mathrm{kg\,s^{-1}}$, **b**, **e** $\dot{m}_{H_2} = 5.0 \times 10^{-6}\,\mathrm{kg\,s^{-1}}$, **c**, **f** $\dot{m}_{H_2} = 1.0 \times 10^{-6}\,\mathrm{kg\,s^{-1}}$. The dominant and secondary modes are characterized by $\omega_1/2\pi$ and $\omega_2/2\pi$ in the frequency spectrum, with units of Hz

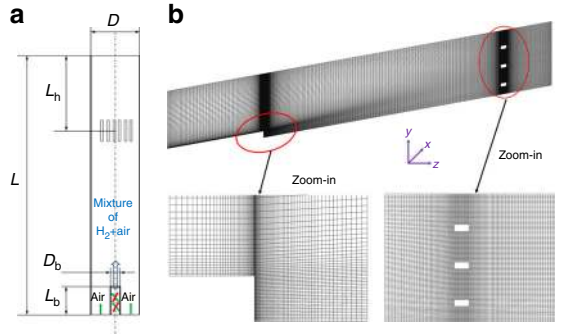

Fig. 8 Schematics and numerical mesh of the open-open combustor with a Bunsen burner confined at the bottom half and heating bands in the top half. **a** Schematics, **b** meshing half of the combustor due to its symmetric structure (bottom embedded two graphs illustrating the zoom-in meshes near the Bunsen burner and the heating bands). The overall axial length is $L = 1000.0$ mm. Inner diameter of the combustor is $D = 50.0$ mm. The height of the Bunsen burner (with respect to bottom open end) is $L_b = 200.00$ mm. The inner diameter of the Bunsen burner is $D_b = 5.0$ mm. The axial distance of the heating bands with respect to top open end is $L_h = 100.00$ mm

where MW_k is the molecular weight of the species k, ν'_k denotes the stoichiometric coefficient for the reactant kth species and ν''_j is the stoichiometric coefficient for the product jth species in the chemical reaction. Further details can be found in ref. [41] or the Fluent documentation, which contains more information about the modelling of the governing equations. A more complex turbulence model[42], e.g. RSM (Reynolds stress model), could have been applied. For comparison, RSM (involving seven equations) is also implemented and evaluated as described in Supplementary Note 6 (Supplementary Figs. 9 and 10). It is shown that the hydrogen-driven pulsating combustion[43] is successfully generated by using either the RSM or the k–ε model. To reduce the computational time and cost, we chose the k–ε turbulence model in the current studies.

Model settings. The essential properties of the computational fluid dynamics (CFD) model are set as follows: (1) a pressure-based coupled solver; (2) unsteady simulations with a time step of $\Delta t = 1.0 \times 10^{-4}$ s and a second-order discretization; (3) a spatial discretization: second-order pressure discretization, and third-order MUSCL scheme for all equations, except the turbulence dissipation (second-order upwind); (4) hydrogen–air mixture (air components: nitrogen (76.8%), oxygen (23.2%) in mass); (5) species transport model, volumetric reactions, eddy-dissipation turbulence–chemistry interaction; (6) a turbulence model: $k-\varepsilon-$RNG; and (7) the gravitational acceleration $g = -9.81\,\mathrm{m\,s^{-2}}$ along the centre line of the open tube.

Boundary conditions arethe following: (a) tube walls are adiabatic; (b) the Bunsen burner wall is adiabatic; (c) heating bands/elements: prescribed constant

temperature (setting $T = 300$ K for $0.0 \le t \le 2.0$, $T = 1300$ K for $2.2\,\mathrm{s} < t$, controlled via UDF (user-defined function); (d) the Bunsen burner tip is a mass flow inlet; (e) the bottom end of the open tube is a pressure inlet (i.e. 0 Pa); (f) the top end of the open tube is a pressure outlet (i.e. 0 Pa). The numerical simulation is started with a flow field as the initial solution, which includes a steady flame, i.e. a flame that is developed in a steady-state simulation. The fuel–air ratio[40] is set to 1.0 for all current simulations. Detailed information is summarized in Supplementary Table 2.

Data post-processing. Short-time Fourier Transform (STFT) is used to analyse the data regarding the acoustic pressure, velocity, and the reaction of heat and heat fluxes. STFT is developed based on the DFT (Discrete Fourier Transform). Let us consider $\mathbf{z}(n)$ as an N-point acquired pressure signal in the time domain $t(N) = N\Delta t$, and let $W_N = \exp(-j2\pi/N)$ and $j = \sqrt{-1}$. The DFT of $z(n)$ is $\mathbf{Z}(n) = \mathrm{DFT}\{\mathbf{z}(n)\}$ is defined as

$$\mathbf{Z}(n) \equiv \sum_{k=0}^{N-1} \mathbf{z}(n) W_N^{nk}, \quad 0 \le i < N \tag{10}$$

Frequency-domain figures are obtained with $\Delta t = 1/10{,}000$ s and $N = 8192$ and a Hamming window.

Data availability

The data that support the findings of this research are available from the corresponding author on request.

Code availability

The code (case files) and data sets generated by using ANSYS FLUENT 15.1 during this study are available from the corresponding author on request.

Received: 9 August 2018 Accepted: 11 March 2019
Published online: 06 May 2019

References

1. Rayleigh, L. The explanation of certain acoustical phenomena. *Nature* **18**, 319–321 (1878).
2. Bragg, S. L. Noise and oscillations in jet engines. *Nature* **201**, 123–129 (1964).
3. Raun, R. L., Beckstead, M. W., Finlinson, J. C. & Brooks, K. P. A review of Rijke tubes Rijke burners and related devices. *Prog. Energy Combust. Sci.* **19**, 313–364 (1993).
4. Hajialigol, N. & Mazaheri, K. Thermal response of a turbulent premixed flame to the imposed inlet oscillating velocity. *Energy* **118**, 209–220 (2017).
5. Zhang, Z., Guan, D., Zheng, Y. & Li, G. Characterizing premixed laminar flame–acoustics nonlinear interaction. *Energy Convers. Manag.* **98**, 331–339 (2015).
6. Zhao, H. et al. Experimental study of equivalence ratio and fuel flow rate effects on nonlinear thermoacoustic instability in a swirl combustor. *Appl. Energy* **208**, 123–131 (2017).
7. Li, J. & Morgans, A. S. Simplified models for the thermodynamic properties along a combustor and their effect on thermoacoustic instability prediction. *Fuel* **184**, 735–748 (2016).
8. Laera, D., Campa, G. & Camporeale, S. M. A finite element method for a weakly nonlinear dynamic analysis and bifurcation tracking of thermo-acoustic instability in longitudinal and annular combustors. *Appl. Energy* **187**, 216–227 (2017).
9. Bauerheim, M. et al. Transmission and reflection of acoustic and entropy waves through a stator–rotor stage. *J. Sound Vib.* **374**, 260–278 (2016).
10. Matsuyama, S. et al. Large-Eddy simulation of high-frequency combustion instability in a single-element atmospheric combustor. *J. Propul. Pow.* **32**(), 628–645 (2016).
11. Hemchandra, S., Shanbhogue, S., Hong, S. & Ghoneim, A. F. Role of hydrodynamic shear layer stability in driving combustion instability in a premixed propane-air backward-facing step combustor. *Phys. Rev. Fluids* **3**, 063201 (2018).
12. Urbano, A. & Selle, L. Driving and damping mechanisms for transverse combustion instabilities in liquid rocket engines. *J. Fluid Mech.* **820**, R2 (2017). https://doi.org/10.1017/jfm.2017.227.
13. Groning, S., Hardi, J. S., Suslov, D. & Oschwald, M. Injector-driven combustion instabilities in a hydrogen/oxygen rocket combustor. *J. Propul. Power* **32**, 560–573 (2016).
14. Kim, Y. J., Lee, D. K. & Kim, Y. Experimental study on combustion instability and attenuation characteristics in the lab-scale gas turbine combustor with a sponge-like porous medium. *J. Mech. Sci. Technol.* **32**, 1879–1887 (2018).
15. Wu, G., Li, S., Zhao, H., Yang, X. L. & Jiaqiang, E. Experimental and frequency-domain study of acoustic damping of single-layer perforated plates. *Aerosp. Sci. Technol.* **69**, 432–438 (2017).
16. Tao, W., Zhang, M. & Li, L. Modeling of acoustic damping of perforations on the combustion instability of annular aero-engine combustors. In *ASME Turbo Expo: Turbomachinery Technical Conference and Exposition*, GT2017–64282, https://doi.org/10.1115/GT2017-64282 (2017).
17. Surendran, A. & Heckl, M. A. Passive instability control by a heat exchanger in a combustor with non-uniform temperature. *Int. J. Spray. Combust.* **9**, 380–393 (2017).
18. Wu, G., Lu, Z. L., Pan, W. C., Guan, Y. H. & Ji, C. Z. Numerical and experimental demonstration of actively passive mitigating self-sustained thermoacoustic oscillations. *Appl. Energy* **222**, 257–266 (2018).
19. Zalluhoglu, U. & Olgac, N. A study of Helmholtz resonators to stabilize thermoacoustically driven pressure oscillations. *J. Acoust. Soc. Am.* **139**, 1962–1973 (2016).
20. Zhang, G. Y., Wang, X. Y., Li, L., Jing, X. D. & Sun, X. F. Control of thermoacoustic instability with a drum-like silencer. *J. Sound Vib.* **406**, 253–276 (2017).
21. Zalluhoglu, U., Kammer, A. S. & Olgac, N. Delayed feedback control laws for Rijke tube thermoacoustic instability, synthesis, and experimental validation. *IEEE T. Contr. Syst. T.* **24**, 1861–1868 (2016).
22. Li, S. et al. Theoretical and experimental demonstration of minimizing self-excited thermoacoustic oscillations by applying anti-sound technique. *Appl. Energy* **181**, 399–407 (2016).
23. Dowling, A. P. & Morgans, A. S. Feedback control of combustion oscillations. *Annu. Rev. Fluid Mech.* **37**, 151–182 (2005).
24. Li, S. et al. Theoretical and experimental demonstration of minimizing self-excited thermoacoustic oscillations by applying anti-sound technique. *Appl. Energy* **181**, 399–407 (2016).
25. Jocher, A., Pitsch, H., Gomez, T., Bonnety, J. & Legros, G. Combustion instability mitigation by magnetic fields. *Phys. Rev. E* **95**, 063113 (2017).
26. Henderson, B. R. & Xu, K. N. G. Electric field damping of Rijke tube combustion instabilities. *J. Propul. Power* **34**, 85–96 (2018).
27. Gopakumar, R., Mondal, S., Paul, R., Mahesh, S. & Chaudhuri, S. Mitigating instability by actuating the swirler in a combustor. *Combust. Flame* **165**, 361–363 (2016).
28. Diao, Q., Ghosh, A. & Yu, K. H. Combustion instability suppression in gaseous oxygen/hydrogen combustors using methane dilution. *J. Propul. Power* **33**, 719–729 (2017).
29. Yilmaz, I., Ratner, A., Ilbas, M. & Huang, Y. Experimental investigation of thermoacoustic coupling using blended hydrogen-methane fuels in a low swirl burner. *Int. J. Hydrog. Energ.* **35**, 329–336 (2010).
30. Choi, O. & Lee, M. C. Investigation into the combustion instability of synthetic natural gases using high speed flame images and their proper orthogonal decomposition. *Int. J. Hydrog. Energ.* **41**, 20731–20743 (2016).
31. Park, J. & Lee, M. C. Combustion instability characteristics of H2/CO/CH4 syngases and synthetic natural gases in a partially-premixed gas turbine combustor: Part I—Frequency and mode analysis. *Int. J. Hydrog. Energ.* **41**, 7484–7493 (2016).
32. Wicksall, D. & Agrawal, A. Acoustics measurements in a lean premixed combustor operated on hydrogen/hydrocarbon fuel mixtures. *Int. J. Hydrog. Energ.* **32**, 1103–1112 (2007).
33. Taamallah, S. et al. Fuel flexibility, stability and emissions in premixed hydrogen-rich gas turbine combustion: technology, fundamentals, and numerical simulations. *Appl. Energy* **154**, 1020–1047 (2015).
34. Qian, C., Bing, W., Huiqiang, Z., Yunlong, Z. & Wei, G. Numerical investigation of H2/air combustion instability driven by large scale vortex in supersonic mixing layers. *Int. J. Hydrog. Energ.* **41**, 3171–3184 (2016).
35. Hoferichter, V. & Sattelmayer, T. Boundary layer flashback in premixed hydrogen-air flames with acoustic excitation. *J. Eng. Gas Turb. Power* **140**, 051502 (2018).
36. Wang, G. Q., Li, Y. Y., Li, L. & Qi, F. Experimental and theoretical investigation on cellular instability of methanol/air flames. *Fuel* **225**, 95–103 (2018).
37. Lee, K., Kim, H., Park, P., Yang, S. & Ko, Y. CO2 radiation heat loss effects on NOx emissions and combustion instabilities in lean premixed flames. *Fuel* **106**, 682–689 (2013).
38. Li, J. X., Xia, Y., Morgans, A. S. & Han, X. S. Numerical prediction of combustion instability limit cycle oscillations for a combustor with a long flame. *Combust. Flame* **185**, 28–43 (2017).
39. Cintra, B. F. C. & Fernandes, E. C. Thermoacoustic instabilities of lean disc flames. *Fuel* **184**, 973–986 (2016).
40. Pires, J. M. & Fernandes, E. C. Combined effect of equivalence ratio and velocity gradients on flame stability and emission formation. *Fuel* **222**, 800–809 (2018).
41. Versteeg, H. K. & Malalasekera, W. *An Introduction to Computational Fluid Dynamics: The Finite Volume Method* (Pearson Education, London, UK, 2007).

42. Zhao, D., Gutmark, E. & de Goey, P. A review of cavity-based trapped vortex, ultra-compact, high-g, inter-turbine combustors. *Progress. Energy Combust. Sci.* **66**, 42–82 (2018).
43. Backhaus, S. & Swift, G. W. A thermoacoustic Stirling heat engine. *Nature* **399**, 335–338 (1999).

Acknowledgements

We gratefully acknowledge the financial support provided by the University of Canterbury, New Zealand (grant no. 452STUPDZ) and National Research Foundation Singapore (grant no. NRF2016NRF-NSFC001-102).

Author contributions

D.Z. and A.R. conducted the numerical computation. D.Z. and Y.G. analysed and discussed the results. D.Z. conceived and initialized the project, and wrote the paper along with Y.G.

Additional information

Supplementary information accompanies this paper at https://doi.org/10.1038/s42005-019-0142-8.

Competing interests: The authors declare no competing interests.